applied sciences

MDPI

Article

Study on Voids and Seepage Characteristics within Rock Fracture after Shear Dislocation Viewing from CT Test and Numerical Modeling

Tingfa Dong [1], Jian Zhou [1,*], Ziqian Yan [1], Yanfang Wu [2] and Tianqiao Mao [3,4]

[1] Faculty of Architecture, Civil and Transportation Engineering, Beijing University of Technology, Beijing 100124, China; dongtingfa@emails.bjut.edu.cn (T.D.); yanziqian0912@163.com (Z.Y.)
[2] School of Mathematics, North University of China, Taiyuan 030051, China; wuyanfang@mail.iggcas.ac.cn
[3] Key Laboratory of Shale Gas and Geoengineering, Institute of Geology and Geophysics, Chinese Academy of Sciences, Beijing 100029, China; maotianqiao@mail.iggcas.ac.cn
[4] Innovation Academy for Earth Science, Chinese Academy of Sciences, Beijing 100029, China
* Correspondence: zhoujian@bjut.edu.cn

Abstract: In rock mass engineering, stress balance changes often cause the relative slip of fractures along a wall surface, impacting the seepage behavior of fluid in the fractures. Using computer tomography (CT) scanning, spatial models of fractures with dislocations ranging from 0 to 10 mm were created to explore the relationship between changes in fracture dislocation and changes in fluid flow behavior, respectively. The spatial fractal dimension of cavity distribution within the fractures was calculated using a thin-plate filling approach to characterize the complexity of the fracture cavity distribution. The fluid flow within the dislocation fractures was then simulated using COMSOL, and the effect of cavity alterations in the form of dislocation on the fluid seepage behavior was analyzed using the spatial fractal. The results show that the values of mechanical aperture after dislocation of the fracture obtained by a CT test are normally distributed, the distribution range of mechanical aperture gradually widens with an increase in the dislocation distance, and the average mechanical aperture increases on a logarithmic curve. The relative spatial fractal dimension decreases gradually with an increase in dislocation distance, and the interconnected pathways within the fracture decrease; in addition, it is observed that the change in the relative spatial fractal dimension is closely correlated with the change in the mean mechanical aperture. Numerical simulations of dislocation fracture seepage found that the permeability increases nonlinearly with increasing dislocation distance. When the dislocation distance reaches 5 mm, nonlinear behaviors such as eddy currents occur, and the influence range of eddy currents gradually expands with the increase in dislocation distance under the influence of the boundary. Moreover, the inertia coefficient B in the Forchheimer equation and the critical hydraulic gradient *Jc*, which can describe the nonlinear seepage characteristics, show a power function decreasing trend with increasing dislocation distance, and the fluid in the fracture is more likely to produce nonlinear flow.

Keywords: fracture shear dislocation; CT scans; seepage numerical simulation; void fractal dimension; nonlinear seepage

check for updates

Citation: Dong, T.; Zhou, J.; Yan, Z.; Wu, Y.; Mao, T. Study on Voids and Seepage Characteristics within Rock Fracture after Shear Dislocation Viewing from CT Test and Numerical Modeling. *Appl. Sci.* **2024**, *14*, 1013. https://doi.org/10.3390/app14031013

Academic Editor: Giuseppe Lacidogna

Received: 22 December 2023
Revised: 17 January 2024
Accepted: 23 January 2024
Published: 24 January 2024

Copyright: © 2024 by the authors. Licensee MDPI, Basel, Switzerland. This article is an open access article distributed under the terms and conditions of the Creative Commons Attribution (CC BY) license (https://creativecommons.org/licenses/by/4.0/).

1. Introduction

Numerous fractures of different scales exist in subsurface rock mass, which controls engineering rock mass' physical, hydrological, and mechanical properties, thus affecting the deformation of surrounding rock, the internal stress distribution, and the seepage characteristics of the surrounding rock mass. Stress balance changes during rock engineering often result in relative sliding along fracture surfaces, altering the fluid permeation behavior within the fractures. For instance, in deep rock engineering applications such as enhanced geothermal system development [1], unconventional oil and gas reservoir exploitation [2], and carbon dioxide sequestration [3], the injection of high-pressure fluids into deep rock mass is employed to expand interconnected fracture pathways, which ultimately constructs a fracture network to enhance energy recovery or increase the storage capacity of deep rock strata. The injection of high-pressure fluids induces changes in the stress field in the rock mass, leading to relative sliding along the fracture surfaces and consequently impacting the flow characteristics. The complexity of fluid flow within the fractures arises from alterations in the stress environment caused by high-pressure fluid injection. As a result, fluid flow within the fractures transitions from linear to nonlinear states, affecting the solute and heat transfer properties within the fractures [4]. Therefore, investigating the changes in permeability characteristics of fluid flow in rock fractures resulting from slip displacement is important.

Studying the deformation and permeability characteristics of a single fracture is a prerequisite for understanding the permeability properties of fractured rock masses [5,6]. Early research on rock fractures assumed that the upper and lower surfaces of fractures were two smooth parallel plates. A cubic law was derived by simplifying the solution to the Navier–Stokes equation, indicating that the fracture's volume flow rate is proportional to the cube of the pressure gradient and the fracture aperture [7]. However, natural fractures are not simple parallel plate structures; they possess a complex rough structure, heterogeneous void distribution, and tortuous geometric shapes. These factors lead to deviations from the cubic law in permeability [8,9], especially when fractures undergo deformation and contact influenced by various factors. This prompts changes in fluid flow velocity or direction within the channels, causing nonlinear fluid flow behaviors such as local eddy currents and turbulence [10]. In contrast to the cubic law, the Forchheimer law describes the nonlinear relationship between pressure gradient and volume flow rate and has been verified in various contexts [11–13]. Rong et al. [14] carried out non-matching flow tests on fractures and found that the Forchheimer equation is highly sensitive to changes in fracture aperture. Zhou et al. [15] proposed a quantitative analysis of the global inertial permeability for the nonlinear term in the Forchheimer equation, characterizing non-Darcy flow in porous media. Therefore, the Forchheimer equation provides an accurate model for describing the nonlinear seepage of mismatched fractures and better understanding the seepage characteristics of fractures under complex conditions.

For a single fracture, its void distribution exhibits complex characteristics closely related to the roughness structure of the fracture surface [16–18]. Scholars usually parameterize the roughness structure of fracture surfaces and analyze its influence on the permeability characteristics of fractures. Parameters include joint roughness coefficients and plane fractal dimensions. By wavelet analysis, Zou et al. [19] divided the fracture surface roughness into primary and secondary roughness. They found that the secondary roughness significantly influences the nonlinear behavior of seepage. Zhang et al. [20] utilized 3D printing technology to create precise samples and conducted seepage tests and numerical simulations. They found that fracture roughness and aperture distribution affect the seepage and pressure fields. On the other hand, characterizing the cavity structure of fractures is also a research focus. Chen et al. [21], through improvements to the cubic covering method, filled the fracture space with ultra-thin square plates, describing the anisotropy of fracture space based on the difference in fractal geometric dimensions between the fracture space and parallel plates with equivalent apertures. However, when fractures undergo shear or slip dislocation under complex stress, the void distribution of fractures undergoes intricate changes with dislocation distance, and different stages have varying impacts on seepage [22,23]. The irregular and unpredictable void distribution of fracture spaces poses a challenge to predicting permeability [10,24]. Researchers have conducted numerous numerical simulations and experimental analyses to explore the seepage characteristics of non-matching fractures [25]. Dang et al. [26] concluded that asperities' influence on aperture changes during the shear process can not be ignored, significantly affecting the seepage characteristics of the fluid in sheared fractures. Xiao et al. [27] summarized coupled shear seepage experiments on fractures, finding that a relatively low-seepage water pressure in the existing test system has a non-negligible impact on the understanding of seepage behavior in a high-stress environment. However, the challenge of maintaining specimen sealing under fracture dislocation conditions in pressure chambers with large shear displacements remains to be addressed and remains a challenge for current research development.

Most current experimental techniques face challenges in directly observing the details of fluid flow in actual rock fractures, especially in profoundly understanding the relationship between local geometric characteristics and seepage behavior in rock fractures [28]. This includes non-linear seepage behaviors such as groove flow [19], eddy current [29], and reflux [30]. Research on observing seepage behavior in fractures typically falls into two methods: destructive observation and non-destructive observation. Among non-destructive observation techniques, computer tomography technology (CT) can accurately obtain data on the distribution of voids in fractures without causing artificial damage to the fracture surfaces [16,31–33]. Using CT technology, Watanabe et al. [34,35] analyzed the flow characteristics of two granite single fracture specimens under confining pressure conditions. They found differences in fracture porosity and permeability under stress influence, but image noise led to insufficient data points. Additionally, based on pore distribution data and numerical simulation methods, the study further investigated the permeability characteristics of actual fractures. This research conclusively confirms the dominant flow behavior within the fractures.

Most of the above studies on fracture seepage are based on rock fractures in the original fracture state. However, there are still insufficient studies on the seepage law of mismatched fractures formed by rock dislocations on both sides of fractures. By combining CT experiments and numerical simulation methods, a more in-depth understanding of the evolution of fluid seepage behavior within non-matching fractures can be achieved. In this study, CT technology was utilized to obtain data on the distribution of voids in single granite fractures at different dislocation distances (0–10 mm). The fracture cavity model corresponding to the dislocation state is established, and the numerical simulation of dislocation fracture seepage is carried out. The parameters are quantified based on the fracture surface morphology data obtained by laser scanning to explore the internal causes of fracture space changes. At the same time, the changes in cavity interconnection channels are investigated through the fracture space structure parameters. Combined with the numerical simulation of seepage velocity field changes, the purpose is to understand further the influence of fracture dislocation state on fluid seepage characteristics.

2. Methods

2.1. Sample Preparation

The Alashan Block is located in the western part of Inner Mongolia, China, and is part of the North China Craton. This region features extensive granite coverage, including Gallidonian granite, Carboniferous granite, and Permian granite. Geological surveys suggest that the Alashan Block may be a favorable candidate for the geological disposal of high-level radioactive waste. For this study, core samples of banded granite from below the surface to a depth of 500 m were collected in the region. The granite is composed of approximately 45% plagioclase, 18% orthoclase, 25% quartz, and about 12% biotite. The grain size distribution of biotite, plagioclase, quartz, and orthoclase is approximately 0.8–1.5 mm, 1.3–3.0 mm, 1.5–4.0 mm, and 2.0–8.0 mm, respectively. The average density of the rock is around 2.65 $\mathrm{g/cm^3}$, with average shear and compressional wave velocities of 3151.8 m/s and 5860.4 m/s, respectively. The banded granite core samples were processed into standard specimens with a diameter of 50 mm and a height of 100 mm. Subsequently, the Brazilian splitting method was employed to split the specimens along the axial direction, obtaining granite samples with rough fractures, as shown in Figure 1a.

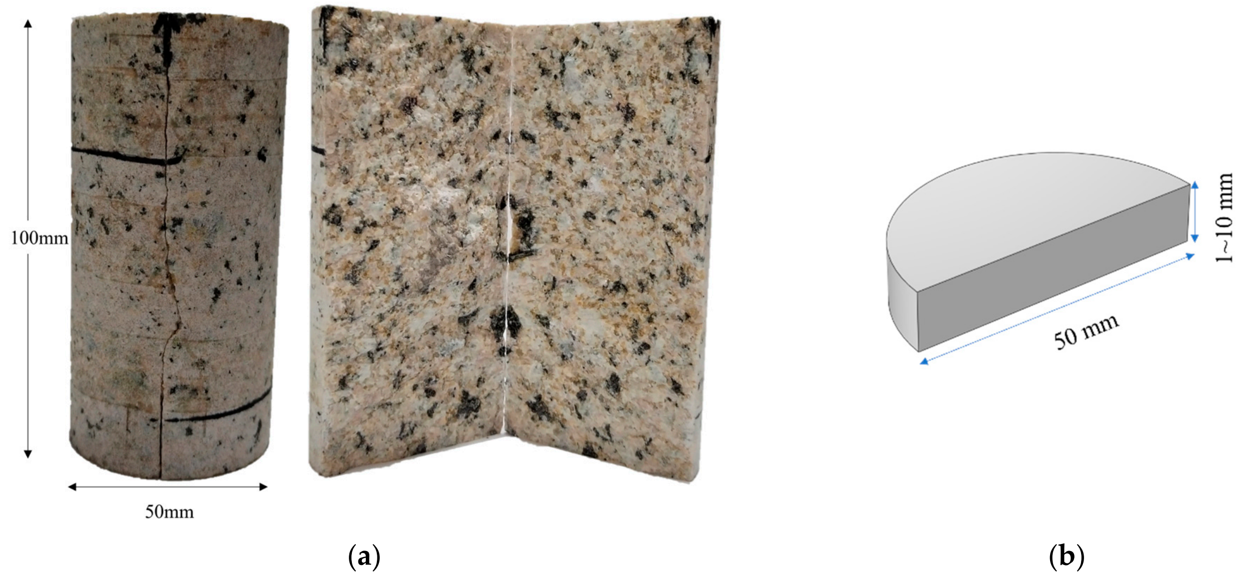

Figure 1. Granite fracture and sample end gasket: (**a**) granite samples with a single fracture surface; (**b**) diagram of gasket for controlling dislocation.

This study focuses on the variation in void distribution caused by rough fractures along a single direction, generated by 0–10 mm shear dislocation, and its impact on seepage characteristics. To ensure the stability of the samples after dislocation during the CT experiments and reduce the artificial dislocation error, semi-cylindrical metal shims with thicknesses ranging from 1 to 10 mm were manufactured based on the geometric characteristics of the samples, as shown in Figure 1b. Two shims of each thickness were prepared and attached to both ends of the samples using glue, resulting in granite fracture samples under 0–10 mm dislocation states.

2.2. Fracture Surface Scanning

To further understand the relationship between the rough structure of the fracture surface and the change in the void when the fracture dislocation occurs, three-dimensional surface morphology data were initially obtained using a 3D laser scanner [36]. The 3D laser scanner employed in this study is the Revopoint MINI, featuring a scanning accuracy of 50 µm and a scanning rate of 10 frames per second, as illustrated in Figure 2. The process of acquiring surface morphology data is outlined below: Before scanning, the 3D laser scanner underwent calibration and adjustment to ensure proper height and angle, enabling the complete recording of the specimen's morphology. Once the scanner was fixed, the specimen was positioned on the tray at an appropriate location. A black accessory that the instrument could not recognize was used to stabilize the specimen, ensuring balance. The scanning program was initiated, where the tray drove the specimen's rotation, collecting point cloud data of the surface morphology of the fracture through scans at various angles. The comprehensive point cloud data of the fracture surface were imported into Geomagic Wrap v. 2021 software for post-processing tasks such as filtering, registration, and merging. This process aimed to create a precise three-dimensional model of the rough fracture surface.

Figure 2. Fracture surface morphology reconstruction by three-dimensional laser scanning.

2.3. CT Tests

Based on the prepared fracture samples, CT experiments were conducted to obtain cavity distribution data of 0–10 mm dislocated fracture samples. The CT scanning experiments relied on a real-time high-energy CT scanning system provided by the Institute of Geology and Geophysics, Chinese Academy of Sciences. This system comprises an X-ray source, detector, rotating platform, pressurization system, and computer, as illustrated in Figure 3. The samples under different shear dislocation conditions were subjected to slice scanning to obtain precise information about the three-dimensional fracture cavities without damaging the specimens, which facilitated the analysis of fracture spatial structure distribution. The test did not consider the effect of stress to minimize the influence of damage accumulation on the dislocation fracture surface under stress conditions on the exploration of nonlinear seepage laws.

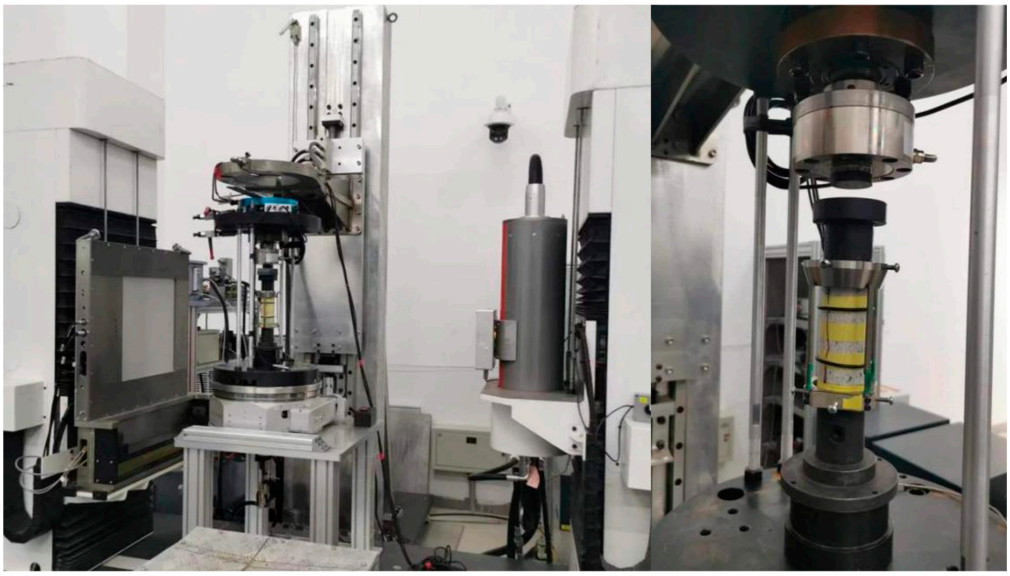

Figure 3. In situ loading high-energy CT real-time scanning system (in Institute of Geology and Geophysics, Chinese Academy of Sciences).

The experimental steps of the CT scanning experiment are as follows: firstly, determining equipment parameters such as imaging range, scanning time, and radiation dose; secondly, fixing the samples in different shear dislocation states using elastic gasket and tape; placing the samples on the scanning bed, and adjusting position as needed to cover the observation area; subsequently, initiating the scanning program, with the X-ray source and detector starting to rotate, capturing a projection image every 0.4°, and recording a series of two-dimensional slice images with a slice thickness of 50 µm. Parameters such as scanning speed, overlap rate, interval, and sampling frequency could be adjusted during the scanning process. After completing the scan, preprocessing steps were applied to eliminate noise and artifacts, including image denoising, enhancement, and filtering using three-dimensional visualization and data analysis software (AVZIO v.2019). Different shear dislocation states fracture cavity spatial models were established, as shown in Figure 4. Subsequently, post-processing was performed based on the established three-dimensional cavity spatial models to enhance model quality.

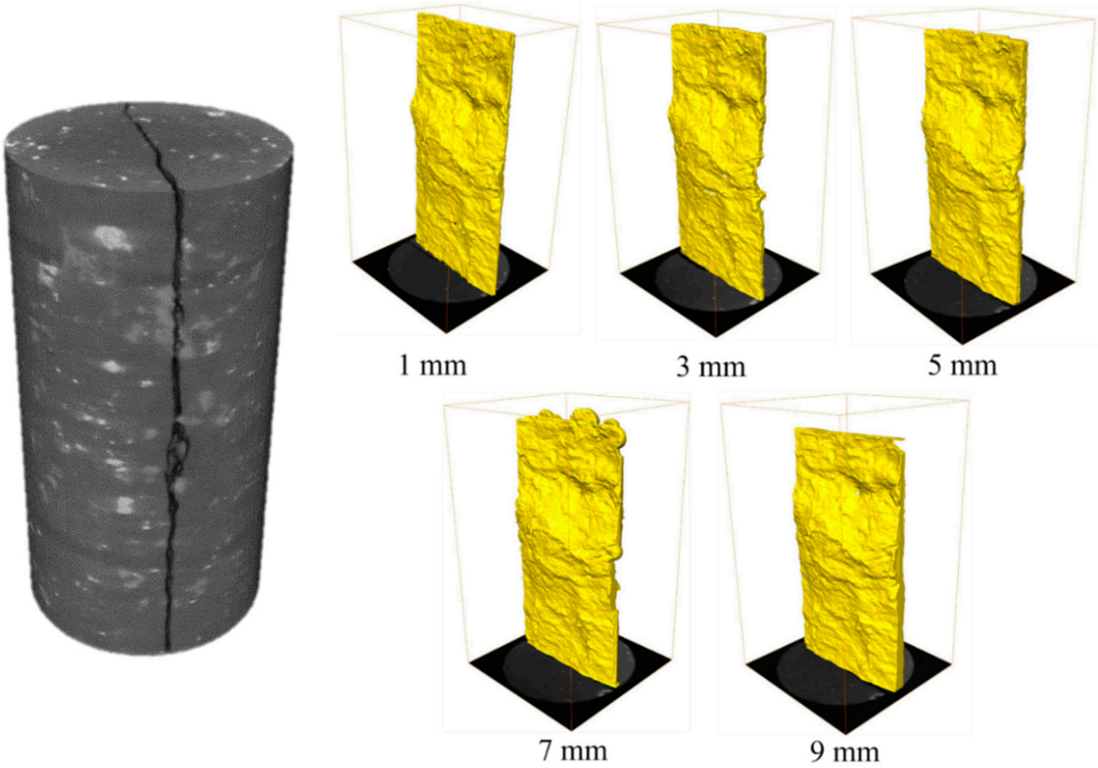

Figure 4. CT reconstruction of rock fracture space with different shear dislocations.

2.4. Fracture Cavity Characterization

The characteristics of rock fractures typically include the morphology of fracture surfaces and the diversity of void changes. Quantifying these characteristics can aid in analyzing the impact of fracture features on seepage. Parameters such as mechanical aperture, fractal dimension, roughness angle, and relative spatial heterogeneity fractal dimension can effectively describe the complexity of fracture surface roughness and the distribution of space void changes. This enables a better understanding of how the structural changes in fracture space, resulting from the uplift of contacted fracture surfaces due to dislocation, influence fluid flow behavior.

Based on the point cloud data obtained from three-dimensional laser scanning of the upper and lower surfaces of the fracture, high-precision grids were fitted with grid intervals of 0.1 mm in the X and Y directions. Therefore, the mechanical aperture of the fracture can be calculated using Equation (1) [37]:

$$e_i = z_i^+ - z_i^- \tag{1}$$

where e_i represents the mechanical aperture at the *i*-th grid node along the fracture dislocation, and $z_i{}^+$ and $z_i{}^-$ denote the spatial heights of the upper and lower fracture surfaces at the corresponding grid node, respectively. Under stress conditions, fracture surfaces typically experience contact closure. In reality, the mechanical aperture of natural fractures cannot be less than zero, and under stress, fracture surfaces tend to come into contact and close. In this study, an aperture size smaller than 50 µm is considered closed. In this closed state, the contribution to fluid flow can be negligible and is treated as a stagnant fluid region [30]. To provide a more intuitive description of the changes in fracture aperture with increasing fault distance, the average mechanical aperture (e_m) is calculated by taking the mean of all mechanical aperture data.

The aperture distribution of fractures reflects the uneven distribution of voids caused by the contact uplift of asperities on the fracture surface. To accurately assess the influence of asperities on fracture aperture, scholars have quantified and investigated the impact of fracture surface roughness on fracture permeability [38–40]. The contact uplift of the fracture surface is primarily related to the friction of the asperities on the fracture surface. Therefore, the roughness angle α of the fracture surface is used to characterize the absolute tilt parameter of the asperities along the dislocation direction, exploring the reasons for the variation in the void distribution with dislocation. The fracture surface roughness angle along the single direction of dislocation can be determined by Equation (2) [41].

$$\tan \alpha_i = \left| \frac{z_{i+1} - z_i}{y_{i+1} - y_i} \right| \tag{2}$$

where z_i and y_i represent the coordinate values on the fracture surface at the corresponding grid node, and *i* is the characterization of the grid nodes of the single profile along the shear direction. The degree of tortuosity of the profile along the single direction is determined by the above equation, based on which the effect of the tortuosity angle of the fracture surface on the change of the fracture dislocation aperture is analyzed.

The roughness angle α_i of the fracture surface describes a single scalar value and is insufficient to characterize the unevenness of the contact and cavity formed by two rough fracture surfaces. Chen et al. [21] made improvements using the cube covering method, filling the fracture space with ultra-thin square plates. The anisotropy of the fracture space is described based on the difference in fractal dimensions between parallel plates with the same opening, as shown in Figure 5. The surface roughness of natural fractures typically follows a self-similar fractal distribution, and the fracture space exhibits self-similarity. The ultra-thin square plate filling method describes interconnected pore space's three-dimensional irregular cavity distribution. The spatial heterogeneity fractal dimension can be obtained by calculating the number of ultra-thin square plates at different side lengths. This parameter reflects the changes in spatial dimension, connectivity, and symmetry. This quantitative method can better understand the complexity and heterogeneity of the fracture space cavity distribution. Based on the above research, the application of spatial fractional dimension can be further expanded to describe the complexity of fracture space cavity distribution under non-matching conditions of fracture surfaces. The specific method is as follows:

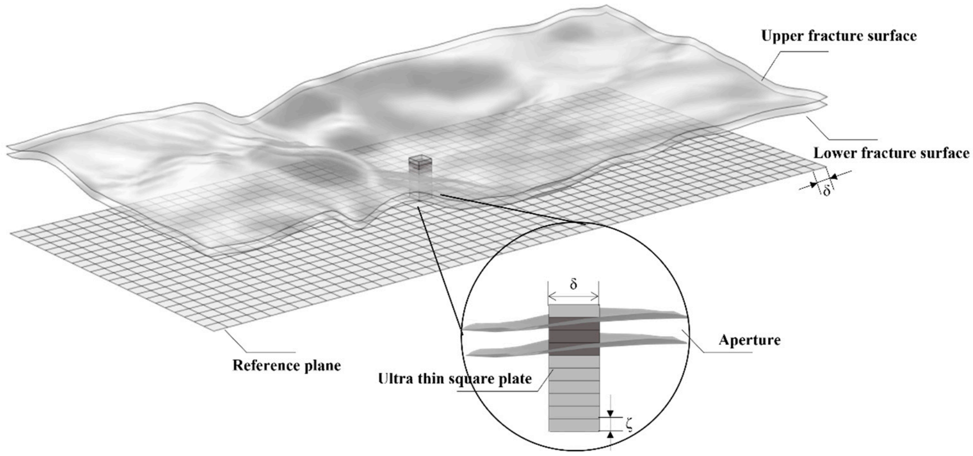

Figure 5. Ultra-thin square plate filling method for the spatial fractional dimension of the void within a fracture.

Based on the high-precision mesh fitting of the actual surface morphology mentioned before, ultra-thin square plates with a width of δ and a thickness of ξ are filled at the mesh nodes. Therefore, the number of thin square plates covering the fracture space at the mesh nodes can be determined by Equation (3).

$$N_{i,j} = INT\left(\frac{\left[\max\left(z^{+}_{(i,j)}, z^{+}_{(i+\delta,j)}, z^{+}_{(i,j+\delta)}, z^{+}_{(i+\delta,j+\delta)}\right) - \max\left(z^{-}_{(i,j)}, z^{-}_{(i+\delta,j)}, z^{-}_{(i,j+\delta)}, z^{-}_{(i+\delta,j+\delta)}\right)\right]}{\xi} + 1\right) \tag{3}$$

where the different elevations of the four mesh nodes are represented by $z_{(i,j)}$ and + and $-$ denote the upper and lower surfaces, respectively. Here, i and j represent the position indices along the width and length directions of the ultra-thin square plate, and $INT(X)$ is the function that returns the largest integer not greater than X. Therefore, the total number of plates filling the entire interconnected fracture space at a given width can be calculated using Equation (4).

$$N_{sum}(\delta) = \sum\nolimits_{i,j=1}^{n-1} N_{i,j} \tag{4}$$

By continuously changing the size of the mesh nodes through Kriging interpolation, the corresponding adjustment of the ultra-thin square plate width δ is made to match the mesh nodes. The total number of ultra-thin square plates also changes accordingly. The relationship between the two can be plotted in a double-logarithmic coordinate system, and the slope of the curve is considered as $-D$, representing the calculated spatial fractal dimension, as shown in Equation (5).

$$-D = \frac{\log_{10} N_{sum}(\delta) - \log_{10} k}{\log_{10} \delta} \tag{5}$$

where k is a proportionality constant, and D represents the corresponding spatial heterogeneous fractional dimension, which describes the heterogeneity of the distribution of interconnected cavity channels in the fracture space. Based on this, by comparing parallel plates with the same mechanical aperture, $D_{\Delta} = D - D^{ref}$ can be obtained. This represents the relative heterogeneous fractional dimension and is used to characterize the complexity of the fracture spatial void distribution.

3. Numerical Simulation of the Seepage of Dislocated Fracture

3.1. Seepage Theoretical Model

The Navier–Stokes equation is generally used to describe fluid motion [38,39]. The steady flow of incompressible fluids can be expressed as Equation (6). The N-S and continuity Equations (6) and (7) are widely used to analyze single fracture flow characteristics [42].

$$\rho(\mathrm{u}\cdot\nabla)\mathrm{u} = -\nabla p + \mu\nabla^2\mathrm{u} \tag{6}$$

$$\nabla\cdot\mathrm{u} = 0 \tag{7}$$

where u represents the velocity vector in m/s, p is the pressure in Pa, ρ is the fluid density in $\mathrm{kg/m^3}$, and μ is the fluid's dynamic viscosity in Pa·s.

With the increase in shear dislocation, the distribution of voids in the fracture space continuously changes, and the fluid in the permeability process is more likely to enter a nonlinear flow state locally. The calculation of nonlinear fluid flow is commonly based on the Forchheimer empirical equation, as shown in Equation (8) [43,44].

$$-\nabla P = \mathrm{A}Q + \mathrm{B}Q^2 \tag{8}$$

where $\bigtriangledown P$ is the pressure gradient, A is the linear term coefficient or viscous term coefficient, and B is the nonlinear term coefficient or inertia coefficient. When the influence of fluid inertia can be neglected at low flow rates, the nonlinear term in the second part ($\mathrm{B}Q^2$) disappears, and the Forchheimer law reduces to Darcy's law. The coefficients A and B are mainly related to the geometric characteristics of the fracture surface tomography [45]. Combining Darcy's law, the permeability of the fracture is calculated through Equation (9) [46]:

$$K = -\frac{Q\mu}{S\nabla P} \tag{9}$$

where K represents the permeability of the fracture, $\mathrm{m^2}$; S is the cross-sectional area of the fracture, $\mathrm{m^2}$.

The dimensionless Reynolds number (Re) is commonly used as an indicator for determining fluid flow regimes, defined as the ratio of inertial forces to viscous forces. For fluid within fractures, Re can be calculated using Equation (10) [22]:

$$Re = \frac{\rho v b_h}{\mu} = \frac{\rho Q}{w\mu} \tag{10}$$

In the equation, b_h represents the hydraulic aperture, and w is the width of the fracture along the direction of the pressure gradient.

3.2. Numerical Models

To investigate the changes in the seepage field of fractured rock masses with displacements ranging from 0 to 10 mm, the single-fracture seepage simulations were conducted based on the fracture cavity model morphology obtained from CT scans under different dislocation conditions. The simulations involved solving the N-S and continuity equations to get the seepage velocity field for dislocation ranging from 0 to 10 mm. The corresponding mesh models are presented in Figure 6. The analysis of cavity variations was combined with the simulation results to understand the causes of complex fluid seepage behavior. In the simulation process, the fluid was assumed to be an incompressible Newtonian fluid with constant density (1×10^3 $\mathrm{kg/m^3}$) and dynamic viscosity (1×10^{-3} Pa·s). The simulation focused on single-phase, saturated, and steady-state conditions for the single-fracture seepage. Considering granite's low porosity and permeability, fluid exchange between the granite matrix and fractures was neglected [46].

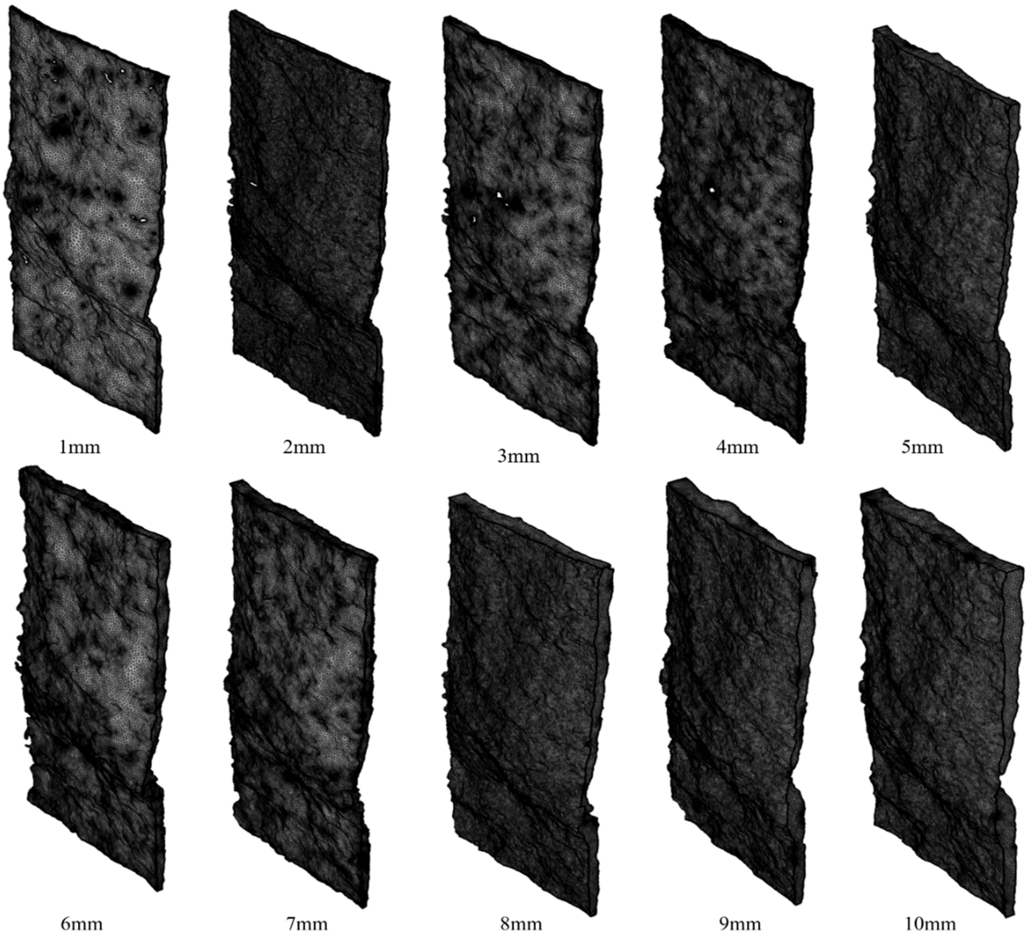

Figure 6. Grid models for the fractures at different dislocations from 1 mm to 10 mm.

Previous experiments and observations have indicated that roughness distribution on the fracture surfaces leads to complex fluid seepage behavior [19]. Solving the three-dimensional N-S equation remains challenging. Under certain conditions, where the fluid is in laminar or creeping flow, i.e., $Re < 2000$, the fracture permeability can be estimated using Darcy's law and the Forchheimer equation [45,47].

COMSOL Multiphysics (https://www.comsol.com/) is a finite element-based multiphysics simulation software widely used for simulating fluid flow in rock fractures. Initially, the models of fractured cavities with various dislocation states are imported into the software. The Y-axis is set along the length of the fracture, the X-axis along the width, and the Z-axis represents the direction of the dislocation-induced uplift, as illustrated in Figure 7. The color filling indicates the local mechanical aperture size of the dislocation-induced fracture.

Subsequently, a network is established for the dislocation-induced fracture space model. COMSOL's built-in mesh generator is employed to generate a discretized mesh automatically suitable for the solver. The mesh is optimized based on the pore size, and the optimal mesh size is selected based on the computation capacity of the workstation. Boundary conditions for the spatial model are then determined according to the physical area. Uniform inlet and outlet boundary conditions are applied to all dislocation fracture models, with the fluid injection flow rate set as the inlet condition (10 mL/s) and the outlet boundary condition set to 0 Pa. The fluid flows primarily along the direction of fracture length under the fluid pressure difference. Other boundaries are treated as no-slip boundary conditions, consistent with many laboratory experimental conditions [12,18].

This study uses COMSOL's laminar flow module to solve the N-S equations. When fluid seepage is simulated, the mesh conditions at the inlet and outlet boundaries are further optimized. A fine mesh with a size of 0.001 mm is used at the inlet and outlet boundaries, while a coarse mesh with a size of 0.1 mm is applied internally. The total number of tetrahedral elements is typically on the order of 10^6. The seepage field for different dislocation states is exported, and the dimensionless Reynolds number Re for fracture flow under different dislocation states is calculated as lower than 300. Thus, the flow regime in the dislocation-induced fractures can be assumed to be linear flow. The permeability of dislocated fracture models can then be calculated by Equation (9).

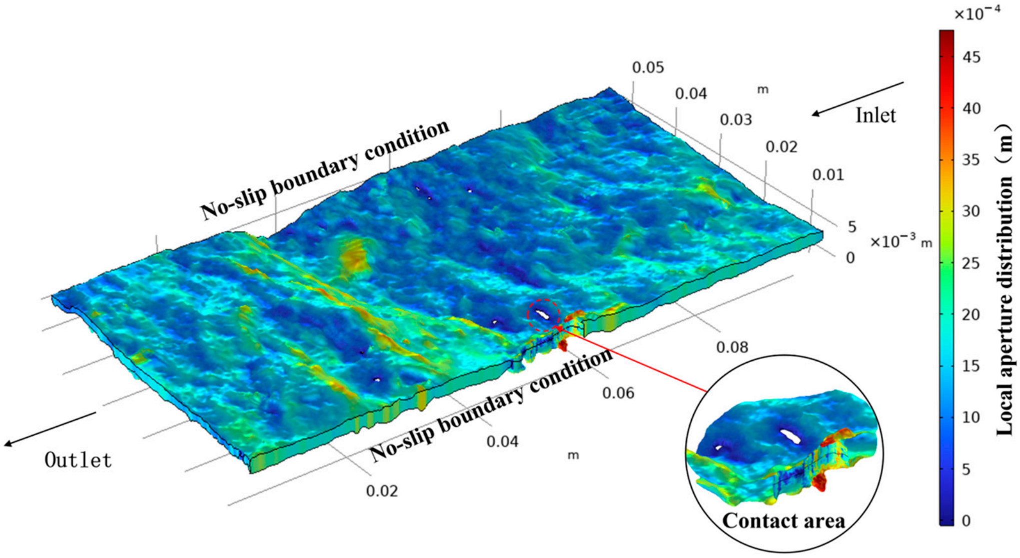

Figure 7. The simulation model of seepage in dislocation fracture, where the color fills in the figure characterize the magnitude of local aperture.

4. Results and Discussion

4.1. Statistics of Fractures' Local Mechanical Aperture Based on CT Data

Figure 8 shows the distribution pattern of local mechanical aperture data with the fracture dislocation distance varying from 0 to 10 mm as a visualization of the variation in the distribution pattern with dislocation distance. The horizontal axis represents the mechanical aperture size, while the vertical axis of each dislocation reflects the amount of corresponding aperture data. It can be observed that with the increase in fracture dislocation distance, the distribution of local mechanical aperture data undergoes a significant evolution from a relatively concentrated distribution in a small aperture to a more extensive local aperture distribution. For instance, when the fracture dislocation is at a distance of 1 mm, the distribution of local mechanical aperture data is relatively narrow, displaying a predominant normal distribution. The local aperture values are primarily concentrated around 1~2 mm. As the fracture dislocation distance increases, the distribution of local aperture data significantly widens. When the fracture dislocation distance reaches 10 mm, most local aperture values are between 1.5 and 3.5 mm.

Figure 9 presents the variation in the average mechanical aperture with fracture dislocation distance under normal stress conditions and stress-free conditions. It is evident that, with the increase in fracture dislocation distance, the average mechanical aperture exhibits nonlinear growth, with the growth rate gradually slowing down, following a logarithmic relationship. This behavior aligns with the experimental and numerical simulation results of Li et al. [47] under normal stress conditions, represented by the red and blue curves in Figure 9. Furthermore, it can be observed that the values of calculated average mechanical aperture e_m do not entirely align with the fitted curve, reflecting the influence of the actual fracture roughness on the average fracture aperture. Compared with the fitting results obtained by Zou et al. [48] through shear experiments, the average mechanical aperture under stress-free conditions is notably lower than the values under certain normal stress conditions.

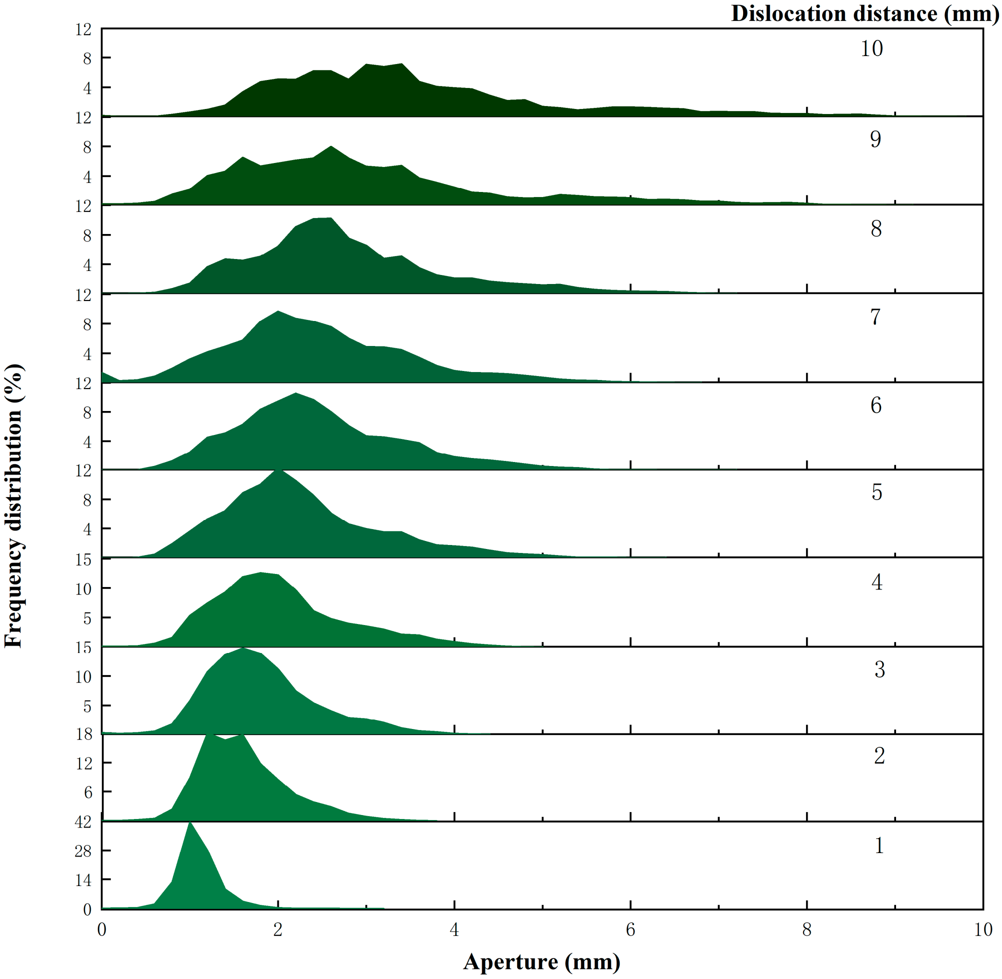

Figure 8. Statistical analysis of fractures' local mechanical aperture.

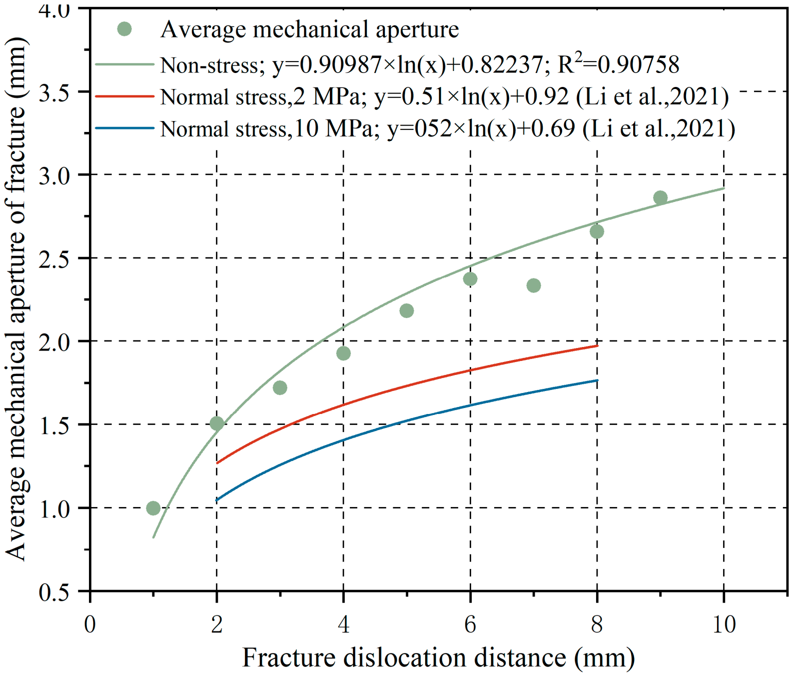

Figure 9. The relationship between the average mechanical aperture of the fracture and the dislocation distance [47].

Considering the curve in the graph variations of the average mechanical aperture e_m with fracture dislocation distance, it can be observed that when dislocation occurs on the fracture surface, the change in fracture aperture generally maintains a certain level. As the fracture dislocation distance increases, the growth of the average mechanical aperture e_m gradually slows down. However, for certain fracture dislocation distances, such as 7 mm and 10 mm, the average mechanical aperture e_m deviates from the curve's growth trend. To better understand the variation in fracture apertures, the roughness angle α is calculated along the length of the rock core in Figure 10. Figure 10a presents a two-dimensional vertical height map of fracture sections along the radial direction of the core, obtained by stacking fracture surface segments taken every 2 mm in the horizontal direction. It shows that the undulation range of the fracture surface is about 4 mm, consistent with the trend of aperture changes when the fracture is uplifted. Figure 10b displays the distribution of the roughness angle along the fracture direction, indicating a relatively gentle variation in roughness angle along the fracture direction, with only local areas exhibiting a more inclined roughness angle.

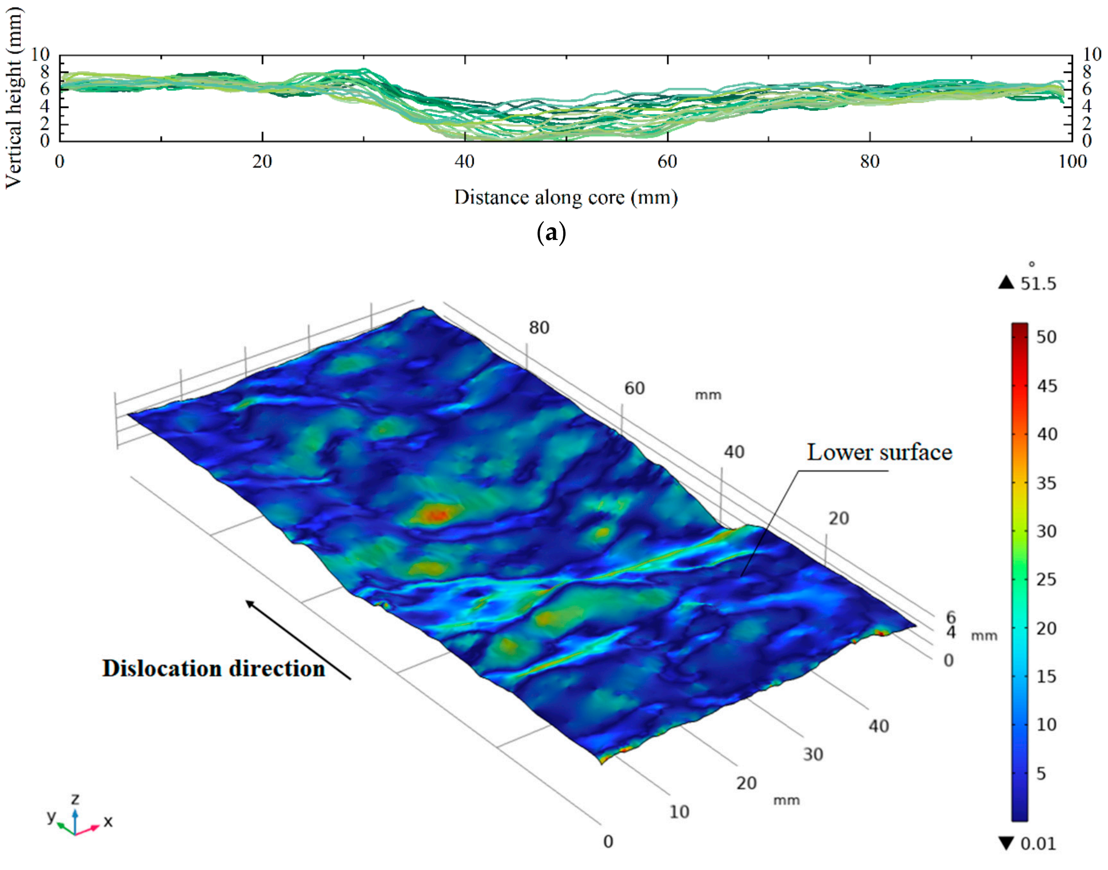

(**a**)

(**b**)

Figure 10. Roughness characteristics of a fracture surface: (**a**) stacking diagram of fracture surface topography in the direction of fracture length; (**b**) absolute roughness angle distribution of fracture surface along the dislocation direction.

Fracture displacement involves altering the void distribution within a fracture and affects the connectivity of void spaces. In this study, MATLAB was employed to code the ultra-thin square plate filling method from Section 2.3 to calculate the relative fractal dimension D_Δ of the fracture void space for fracture displacements ranging from 1 to 10 mm. This was carried out to assess spatial complexity changes resulting from fracture displacement variations. The ultra-thin square plate filling method is closely related to the selected thickness of the plates. This research chose four thicknesses, namely 0.1 mm, 0.2 mm, 0.3 mm, and 0.4 mm [5]. Subsequently, a log–log plot was established between the number of ultra-thin square plates and square plate width, and the curve equation was fitted. The coefficient of the linear term in the curve fitting equation represents the calculated spatial fractal dimension. The spatial fractal dimension D was then subtracted from the fractal dimension of void space with the same mechanical aperture, and the relative spatial fractal dimension was obtained. The relationship between the relative spatial fractal dimension D_Δ and fracture dislocation distance is shown in Figure 11, where some of the fracture cavity complex variations are labeled in the figure. At the beginning of the curve, the distribution of fracture voids approaches that of parallel plates with the same mechanical aperture, indicating a reduction in void connectivity and a decrease in fracture complexity. As fracture displacement changes, it can be observed that the relative spatial fractal dimension of the fracture exhibits nonlinear growth. Specifically, at 3 mm and 7 mm fracture displacements, the relative spatial fractal dimension D_Δ deviates from the curve, smaller than the predicted relative spatial fractal dimensions. Figure 6 shows that the 3 mm dislocation fracture model has more contacts and widespread aperture distribution, resulting in a relatively complex fracture void distribution. Regarding the spatial fractal dimension variation in the model of 7 mm dislocation, combined with the 7 mm fracture void model in Figure 6 and the average mechanical aperture changes in Figure 7, it is inferred that the decrease in D_Δ is due to a local reduction in fracture aperture, leading to an increase in void connectivity and an overall increase in complexity.

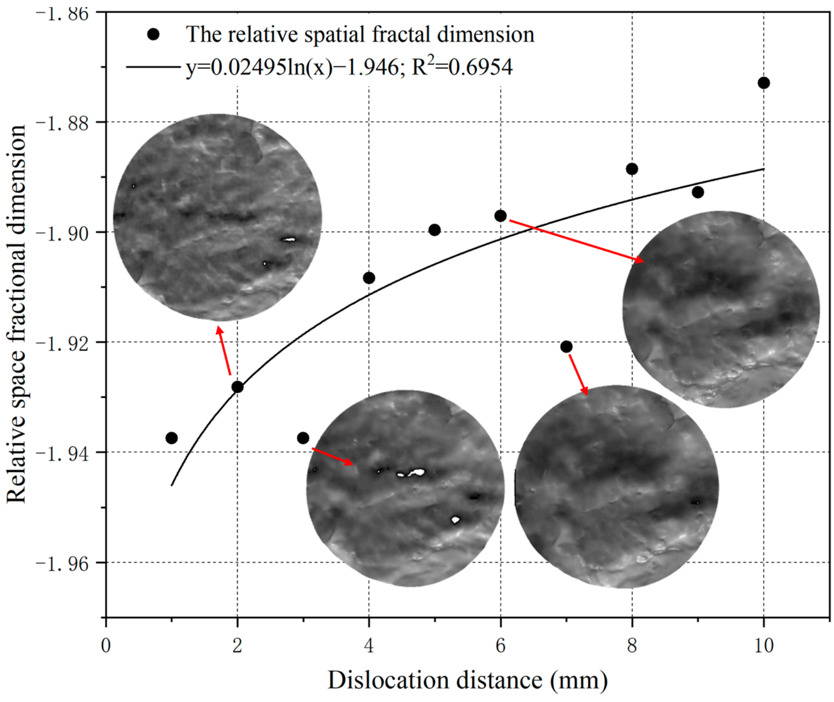

Figure 11. The relationship between fracture spatial fractal dimension and dislocation distance. (The red arrow leads to a comparison of fracture openings).

4.2. Seepage Velocity Field Analysis of Dislocation Fracture

Figure 12 presents the curve of the fracture permeability K as a function of fracture displacement d. The graph shows that with the increase in fracture displacement d, the fracture permeability K shows a nonlinear growth trend, and the growth trend slows down. This trend is consistent with the results obtained by Li et al. [47] in experiments and simulations of fracture shear seepage under normal stress conditions. Under stress conditions, fracture shear mainly occurs in the compaction stage, and the fracture aperture changes relatively little with fracture displacement, resulting in nonlinear growth in permeability K, which eventually tends to flatten. When fractures experience fracture displacement under stress-free conditions, the average mechanical aperture of the fractures is more significant than that under stress conditions. Similarly, the change in permeability K is more important than that under stress conditions, especially after the fracture displacement exceeds 5 mm, where the permeability is twice that of the shear permeability under stress conditions. Figure 12 shows that when the fracture displacement is 7 mm, the fracture permeability K deviates from the curve, and the permeability is lower than that under previous fracture displacement states. This is closely related to the increase in fracture complexity mentioned in Section 4.1. Further analysis of the fracture flow velocity field is conducted to understand better the relationship between permeability K and the void space variation caused by fracture displacement. Table 1 summarizes the parameters analyzed for the flow velocity field.

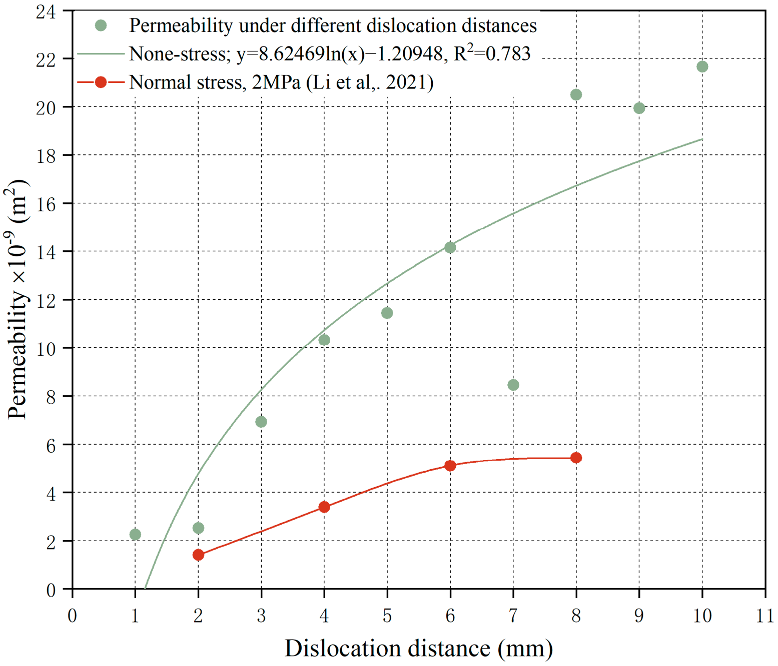

Figure 12. Fracture permeability changing with dislocation distance [47].

Table 1. Seepage velocity field parameters for different dislocation fractures.

Dislocation Distance d/mm	Nonliner Factor E	Critical Hydraulic Gradient $J_c \times 10^3$/Pa	Inertia CoefficientB $\times 10^{11}$/Pa $\times$ S^2 $\times$ m^2	Seepage Pressure Gradient ΔP/Pa	Reynolds Number Re
1	0.56	5.58	55.81	1006.5	210.53
2	0.52	2.04	20.37	393.47	210.53
3	0.54	1.80	17.96	329.6	211.75
4	0.45	0.91	9.14	204.6	214.4
5	0.58	0.82	8.24	143.1	222.61
6	0.51	0.63	6.33	124.8	217.42
7	0.59	0.75	7.52	128.8	215.98
8	0.55	0.55	5.53	100.3	224.78
9	0.60	0.62	6.19	103.9	216.92
10	0.63	0.27	2.65	41.9	217.87

Figure 13 illustrates the distribution of the flow velocity field in fractures at various fracture displacements, with 400 streamlines set at the inlet. A grayscale map of the local aperture distribution is filled on the lower surface to provide a more intuitive understanding of the influence of fracture displacement on fluid flow. Figure 13 shows that the flow velocity within the fracture gradually decreases with increasing fracture displacement and exhibits a distinct preferential flow phenomenon, with streamlines avoiding areas of smaller local apertures. Additionally, as the fault displacement d gradually increases from 1 mm to 4 mm, the contact between fracture surfaces along the Y-axis at approximately 70 mm gradually occurs, increasing the contact area. When the fracture displacement d increases from 5 mm to 10 mm, the contact region along the Y-axis at 70 mm becomes a lower aperture, and the aperture distribution becomes complex and variable. Considering the flow velocity field at various fracture displacements, it is observed that the mechanical apertures are more extensive along the Y-axis at 40 mm compared to other regions. When the fracture displacement d increases from 3 mm to 10 mm, vortices and other nonlinear phenomena occur in the fracture at approximately 40 mm and 70 mm along the Y-axis. The occurrence of nonlinear phenomena is closely related to the contact state and shape of the fracture surfaces. For example, when the fracture displacement is 3 mm, the contact area of the fracture surface is more significant than that at a 2 mm fracture displacement and exhibits an irregular distribution. The increase in the relative spatial fractal dimension D_Δ leads to fluid accumulation and pressure at smaller apertures, forming vortices after contact points. This is consistent with the understanding of nonlinear behavior in flow presented by Lee et al. [10]. The right-upward causes the vortex at 40 mm along the Y-axis inclined geometric structure with a 10° inclination, and it is influenced by the boundary shape, resulting in a flow direction change and the formation of a vortex. Regarding the deviation of the permeability K from the growth trend in Figure 11 when the fracture displacement d is 7 mm, in addition to the increased complexity indicated by the relative spatial fractal dimension D_Δ, the development area of the vortex is much larger than that in the flow velocity field at other fracture displacements. This is because at this fracture displacement, the larger aperture at 40 mm along the Y-axis occupies a larger area. Considering the variation in the fracture flow velocity field with fracture displacement d in Figure 13, it can be seen that the influence range of the vortex gradually expands with increasing fracture displacement, and it is affected by the boundary shape and fracture surface structure, impacting the development of permeability K.

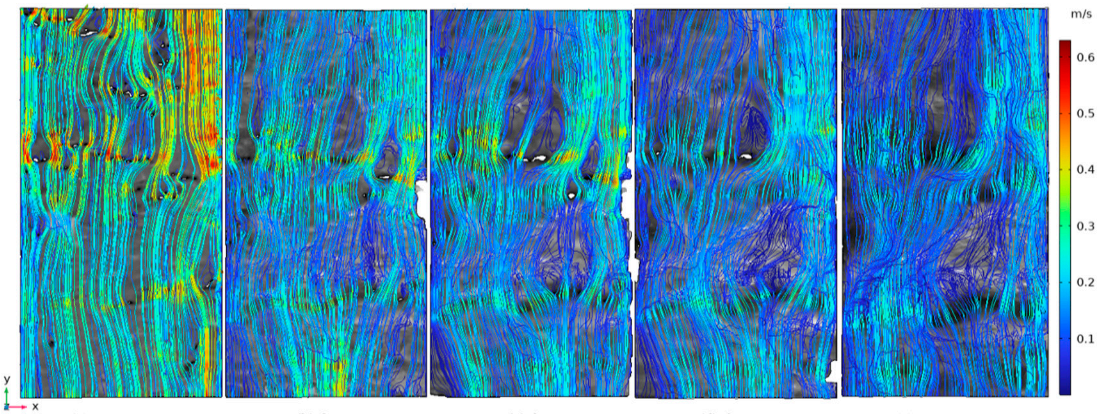

(a) 1mm (b) 2mm (c) 3mm (d) 4mm (e) 5mm

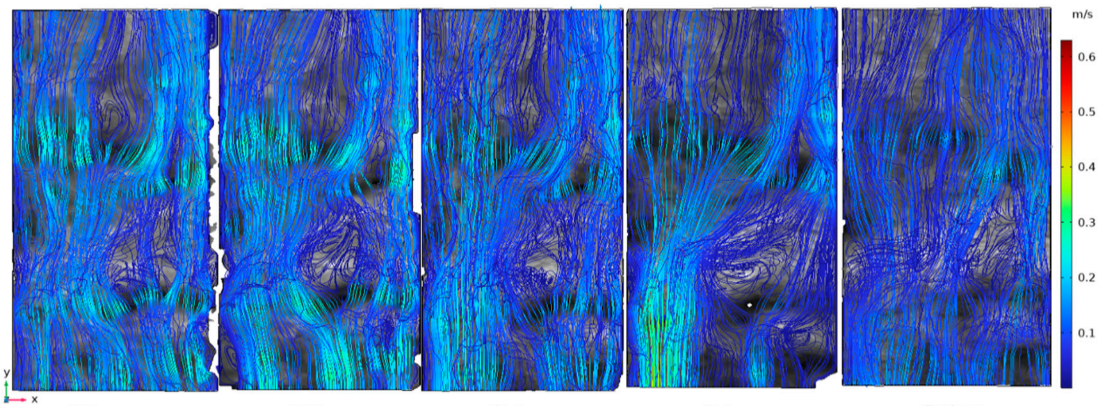

(f) 6mm (g) 7mm (h) 8mm (i) 9mm (j) 10mm

Figure 13. Distribution of flow velocity field under different dislocation distances of fractures.

Although the Reynolds number *Re* is lower than 300 in Table 1, the fluid velocity fields in Figure 13 show a century non-linear behavior. To better understand the nonlinear changes in the process of fracture seepage, the nonlinear factor E is introduced as in [49]:

$$E = \frac{\mathrm{B}Q^2}{\mathrm{A}Q + \mathrm{B}Q^2} \tag{11}$$

This parameter quantifies the proportion of nonlinear behavior in the overall seepage process, providing a comprehensive perspective for understanding the complexity of fracture seepage. When the nonlinear factor E is set to 0.1, the fluid transitions from linear to nonlinear states [50], and the corresponding critical hydraulic gradient is defined as the critical hydraulic gradient J_c [51]. The Forchheimer equation is employed in describing the nonlinear flow characteristics of fracture seepage. The parameters of this equation have distinct meanings, where A represents the intrinsic permeability of the fracture, and B is considered a crucial parameter for describing nonlinear flow [15,18,45]. Therefore, an analysis of the variations in the critical hydraulic gradient J_c and the inertial coefficient B with the fracture displacement is presented in Figure 14.

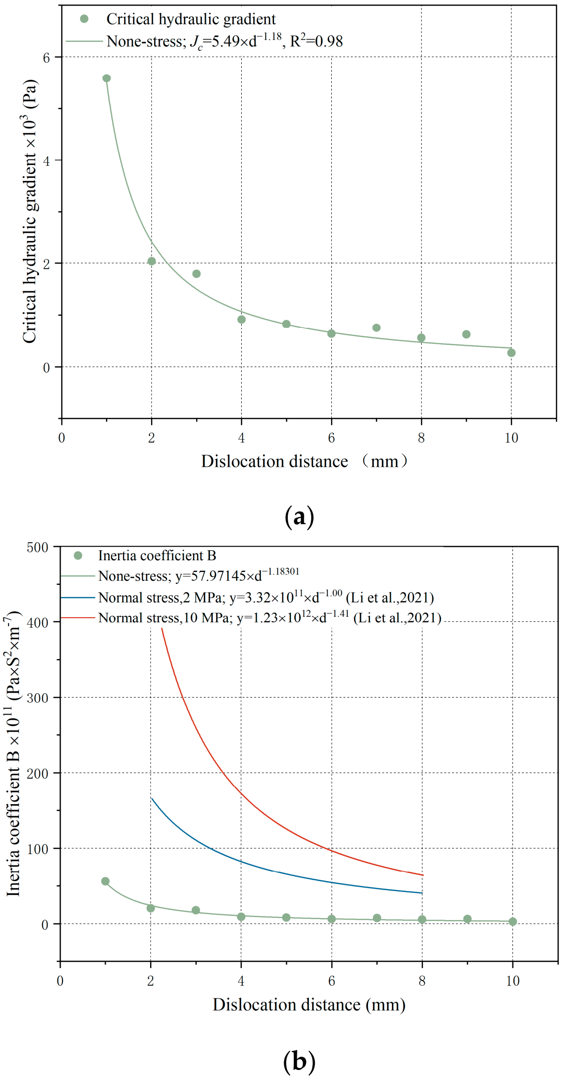

Figure 14. The relationship between critical hydraulic gradient and inertia coefficient with fracture dislocation distance: (**a**) variation with the critical hydraulic gradient of dislocation distance; (**b**) variation with the inertial coefficient B of dislocation distance [47].

Figure 14 shows that with the increase in fracture displacement d, the critical hydraulic gradient J_c and the inertial coefficient B exhibit a gradually decreasing power–law relationship. The rate of decrease gradually slows down, and the nonlinear factor E under different fracture displacements is consistently greater than 0.1. This indicates that fracture seepage predominantly manifests as nonlinear seepage in this study. Figure 14b illustrates the variation in the inertial parameter B of the Forchheimer equation with fracture displacement d. The curve's form aligns with the results of other researchers and is smaller than the seepage under shear conditions when the fracture experiences stress. This is because the average aperture change when the fracture undergoes displacement is more significant than the aperture change under shear conditions with stress, making fracture seepage less prone to becoming nonlinear, manifested in the curve as a reduction in the inertial coefficient B. As the fracture displacement d increases, the fluid becomes less inclined to exhibit nonlinearity. It is noteworthy that, as indicated by the flow field distribution, even in cases of relatively small nonlinear coefficients, complex fluid behaviors such as vortices may still occur during the seepage process [10], as shown in Figure 13d. This suggests that the nonlinear coefficient does not necessarily preclude the occurrence of other complex flow phenomena during the seepage process; instead, it is used to quantify the proportion of nonlinear phenomena in the overall seepage. Therefore, considering both the nonlinear coefficient and the velocity field distribution comprehensively enhances our understanding of the complexity of fracture seepage.

5. Conclusions

In this study, CT scans were employed to investigate the void distribution of actual fractures under different fracture dislocation distance states. Spatial variations of void during the fracture dislocation distance process were analyzed based on parameters such as average mechanical aperture, relative spatial fractal dimension, and fracture surface roughness angle distribution. Subsequently, numerical fluid flow simulations were conducted based on the fracture void models obtained from CT experiments at different fracture dislocation distances. The impact of fracture dislocation on fracture permeability and the nonlinear behavior of fluid flow was analyzed. The main conclusions are as follows:

(1) Fracture dislocation significantly influences aperture distribution. The aperture frequency distribution obtained from CT experiments exhibits a normal distribution. As the fracture dislocation distance increases, the numerical range of the local aperture gradually transitions from relatively narrow to broader, and the maximum local aperture of fractures increases. The average mechanical aperture (e_m) growth follows a logarithmic function and is closely related to the roughness angle of the fracture surface.

(2) The average mechanical aperture and the distribution of local apertures during fracture dislocation affect the complexity of void connectivity. With increasing fracture dislocation distance, the relative spatial fractal dimension (D_Δ) of fractures shows a logarithmic relationship, indicating a decrease in void connectivity and a reduction in the complexity of the fluid flow pathways.

(3) The fracture permeability increases nonlinearly with the increase in dislocation distance. Under the same injection flow rate, the seepage flow in the fracture changes from linear flow to nonlinear flow, and the dominant flow linear flow in dislocation fracture is very obvious. When the dislocation distance reaches 5 mm, nonlinear behaviors such as eddy currents occur, and the influence range of eddy currents gradually expands with the increase in dislocation distance. The fracture surface morphology structure as the boundary of seepage has a significant influence on the seepage behavior. It is also found that the change in dislocation fracture permeability with dislocation distance is closely related to the change in spatial fractal dimension.

(4) With the increase in dislocation distance, the critical hydraulic gradient J_c and the inertia coefficient B, which distinguish linear and nonlinear flows, show a power function decrease and gradually tend to a stable value, indicating that the fluid in the fracture is more likely to produce nonlinear flow with the increase in dislocation

distance. The degree of distribution of the cavity is gradually reduced, and the fluid presents a dominant flow, which enhances the nonlinear ability of fluid in the fracture. The inertia coefficient B and the critical hydraulic gradient J_c in the Forchheimer equation can quantitatively describe the nonlinear seepage characteristics of the fracture.

In summary, this study reveals the influence of fracture dislocation on fluid flow characteristics through a combination of CT experiments and numerical simulations. This research holds crucial significance for understanding the nonlinear behavior of fracture flow and the impact of fracture dislocation on permeability, providing a more profound perspective for fracture flow studies. Further studies are still needed on the effects of different fracture morphologies and the seepage–flow coupling of fracture shear processes.

Author Contributions: Conceptualization, J.Z.; methodology, J.Z. and T.D.; software, T.D. and Y.W.; validation, T.D., T.M. and Y.W.; formal analysis, T.D.; writing—original draft preparation, J.Z., T.D. and Z.Y.; writing—review and editing, J.Z. All authors have read and agreed to the published version of the manuscript.

Funding: This research is supported by funding from the National Natural Science Foundation of China (Grant Nos. 42277144, 41972287).

Data Availability Statement: All the data required to evaluate the conclusions of this study are present in the paper. The authors will provide additional data related to this paper upon request. The data are not publicly available due to privacy.

Conflicts of Interest: The authors declare no conflicts of interest.

References

1. Gischig, V.S.; Giardini, D.; Amann, F.; Hertich, M.; Krietsch, H.; Loew, S.; Maurer, H.; Villiger, L.; Wiemer, S.; Bethmann, F.; et al. Hydraulic stimulation and fluid circulation experiments in underground laboratories: Stepping up the scale towards engineered geothermal systems. *Geomech. Energy Environ.* **2020**, *24*, 100175. [CrossRef]
2. Reedy, R.C.; Nicot, J.-P.; Scanlon, B.R. Comparison of Water Use for Hydraulic Fracturing for Unconventional Oil and Gas versus Conventional Oil. *Environ. Sci. Technol.* **2014**, *48*, 12386–12393.
3. Lima, M.G.; Schädle, P.; Green, C.P.; Vogler, D.; Saar, M.O.; Kong, Z. Permeability Impairment and Salt Precipitation Patterns during CO_2 Injection into Single Natural Brine-Filled Fractures. *Water Resour. Res.* **2020**, *56*, e2020WR027213. [CrossRef]
4. Tan, J.; Rong, G.; He, R.; Yang, J.; Peng, J. Numerical investigation of heat transfer effect on flow behavior in a single fracture. *Arab J Geosci.* **2020**, *13*, 851. [CrossRef]
5. Chen, Y.D.; Selvadurai, A.P.S.; Zhao, Z. Modeling of flow characteristics in 3D rough rock fracture with geometry changes under confining stresses. *Comput. Geotech.* **2021**, *130*, 103910. [CrossRef]
6. Chen, Y.; Lian, H.; Liang, W.; Yang, J.; Nguyen, V.P.; Bordas, S.P.A. The influence of fracture geometry variation on non-Darcy flow in fractures under confining stresses. *Int. J. Rock Mech. Min. Sci.* **2019**, *113*, 59–71. [CrossRef]
7. Snow, D.T. Anisotropie permeability of fractured media. *Water Resour. Res.* **1969**, *5*, 1273–1289. [CrossRef]
8. Witherspoon, P.A.; Wang, J.S.Y.; Iwai, K.; Gale, J.E. Validity of cubic law for fluid flow in a deformable rock fracture. *Water Resour. Res.* **1980**, *16*, 1016–1024. [CrossRef]
9. Cunningham, D.; Auradou, H.; Shojaei-Zadeh, S.; Drazer, G. The effect of fracture roughness on the onset of nonlinear flow. *Water Resour. Res.* **2020**, *56*, e2020WR028049. [CrossRef]
10. Lee, S.H.; Lee, K.K.; Yeo, I.W. Assessment of the validity of Stokes and Reynolds equations for fluid flow through a rough-walled fracture with flow imaging. *Geophys. Res. Lett.* **2014**, *41*, 4578–4585. [CrossRef]
11. Chen, Y.F.; Zhou, J.Q.; Hu, S.H.; Hu, R.; Zhou, C.B. Evaluation of Forchheimer equation coefficients for non-Darcy flow in deformable rough-walled fractures. *J. Hydrol.* **2015**, *529*, 993–1006. [CrossRef]
12. Rong, G.; Hou, D.; Yang, J.; Cheng, L.; Zhou, C. Experimental study of flow characteristics in non-mated rock fractures considering 3D definition of fracture surfaces. *Eng. Geol.* **2017**, *220*, 152–163. [CrossRef]
13. Tzelepis, V.; Moutsopoulos, K.N.; Papaspyros, J.N.E.; Tsihrintzis, V.A. Experimental investigation of flow behavior in smooth and rough artificial fractures. *J. Hydrol.* **2015**, *521*, 108–118. [CrossRef]
14. Rong, G.; Yang, J.; Cheng, L.; Zhou, C. Laboratory investigation of nonlinear flow characteristics in rough fractures during shear process. *J. Hydrol.* **2016**, *541*, 1385–1394. [CrossRef]
15. Zhou, J.Q.; Gan, F.S.; Li, C.; Tang, H. A global inertial permeability for fluid flow in rock fractures: Criterion and significance. *Eng. Geol.* **2023**, *322*, 107167. [CrossRef]
16. Huo, D.; Benson, S.M. Experimental Investigation of Stress-Dependency of Relative Permeability in Rock Fractures. *Transp. Porous Media* **2016**, *113*, 567–590. [CrossRef]

17. Zhang, Z.; Nemcik, J. Fluid flow regimes and nonlinear flow characteristics in deformable rock fractures. *J. Hydrol.* **2013**, *477*, 139–151. [CrossRef]
18. Zoorabadi, M.; Saydam, S.; Timms, W.; Hebblewhite, B. Non-linear flow behaviour of rough fractures having standard JRC profiles. *Int. J. Rock Mech. Min. Sci.* **2015**, *76*, 192–199. [CrossRef]
19. Zou, L.; Jing, L.; Cvetkovic, V. Roughness decomposition and nonlinear fluid flow in a single rock fracture. *Int. J. Rock Mech. Min. Sci.* **2015**, *75*, 102–118. [CrossRef]
20. Zhang, Y.; Ye, J.; Li, P. Flow Characteristics in a 3D-Printed Rough Fracture. *Rock Mech. Rock Eng.* **2022**, *55*, 4329–4349. [CrossRef]
21. Chen, Y.; Liang, W.; Lian, H.; Yang, J.; Nguyen, V.P. Experimental study on the effect of fracture geometric characteristics on the permeability in deformable rough-walled fractures. *Int. J. Rock Mech. Min. Sci.* **2017**, *98*, 121–140. [CrossRef]
22. Javadi, M.; Sharifzadeh, M.; Shahriar, K.; Mitani, Y. Critical Reynolds number for nonlinear flow through rough-walled fractures: The role of shear processes. *Water Resour. Res.* **2014**, *50*, 1789–1804. [CrossRef]
23. Karimzade, E.; Cheraghi Seifabad, M.; Sharifzadeh, M.; Baghbanan, A. Modelling of Flow–Shear Coupling Process in Rough Rock Fractures Using Three-Dimensional Finite Volume Approach. *Rock Mech. Rock Eng.* **2019**, *52*, 4693–4713. [CrossRef]
24. Xiong, X.; Li, B.; Jiang, Y.; Koyama, T.; Zhang, C. Experimental and numerical study of the geometrical and hydraulic characteristics of a single rock fracture during shear. *Int. J. Rock Mech. Min. Sci.* **2011**, *48*, 1292–1302. [CrossRef]
25. Liu, R.; He, M.; Huang, N.; Jiang, Y.; Yu, L. Three-dimensional double-rough-walled modeling of fluid flow through self-affine shear fractures. *J. Rock Mech. Geotech. Eng.* **2020**, *12*, 41–49. [CrossRef]
26. Dang, W.; Wu, W.; Konietzky, H.; Qian, J. Effect of shear-induced aperture evolution on fluid flow in rock fractures. *Comput. Geotech.* **2019**, *114*, 103152. [CrossRef]
27. Xiao, W.; Xia, C.; Deng, R. Research progress on stress-permeability coupling experimental system for rock joints. *J. Rock Mech. Eng.* **2014**, *33*, 3456–3465. (In Chinese) [CrossRef]
28. Phillips, T.; Bultreys, T.; Bisdom, K.; Kampman, N.; Offenwert, S.V.; Mascini, A.; Cnudde, V.; Busch, A. A Systematic Investigation into the Control of Roughness on the Flow Properties of 3D-Printed Fractures. *Water Resour. Res.* **2021**, *57*, ewrcr.25233. [CrossRef]
29. Zhou, J.Q.; Wang, L.; Chen, Y.F.; Cardenas, M.B. Mass transfer between recirculation and main flow zones: Is physically based parameterization possible? *Water Resour. Res.* **2019**, *55*, 345–362. [CrossRef]
30. Javanmard, H.; Ebigbo, A.; Walsh, S.D.C.; Saar, M.O.; Vogler, D. No-Flow Fraction (NFF) permeability model for rough fractures under normal stress. *Water Resour. Res.* **2021**, *57*, e2020WR029080. [CrossRef]
31. Wanniarachchi, W.A.M.; Ranjith, P.G.; Perera, M.S.A.; Rathnaweera, T.D.; Zhang, D.C.; Zhang, C. Investigation of effects of fracturing fluid on hydraulic fracturing and fracture permeability of reservoir rocks: An experimental study using water and foam fracturing. *Eng. Fract. Mech.* **2018**, *194*, 117–135. [CrossRef]
32. Ketcham, R.A.; Slottke, D.T.; Sharp, J.M., Jr. Three-dimensional measurement of fractures in heterogeneous materials using high-resolution X-ray computed tomography. *Geosphere* **2010**, *6*, 499–514. [CrossRef]
33. Kling, T.; Huo, D.; Schwarz, J.O.; Schwarz, J.O.; Enzmann, F.; Benson, S.M.; Blum, P. Simulating stress-dependent fluid flow in a fractured core sample using real-time X-ray CT data. *Solid Earth* **2016**, *7*, 1109–1124. [CrossRef]
34. Watanabe, N.; Ishibashi, T.; Ohsaki, Y.; Tsuchiya, Y.; Tamagawa, T.; Hirano, N.; Okabe, H.; Tsuchiya, N. X-ray CT based numerical analysis of fracture flow for core samples under various confining pressures. *Eng. Geol.* **2011**, *123*, 338–346. [CrossRef]
35. Watanabe, N.; Ishibashi, T.; Hirano, N.; Tsuchiya, N.; Ohsaki, Y.; Tamaqawa, T.; Tsuchiya, Y.; Okabe, H. Precise 3D numerical modeling of fracture flow coupled with X-ray computed tomography for reservoir core samples. *SPE J.* **2011**, *16*, 683–691. [CrossRef]
36. Li, Y.; Chen, Y.F.; Zhou, C.B. Hydraulic properties of partially saturated rock fractures subjected to mechanical loading. *Eng. Geol.* **2014**, *179*, 24–31. [CrossRef]
37. Wang, M.; Chen, Y.F.; Ma, G.W.; Zhou, J.Q.; Zhou, C.B. Influence of surface roughness on nonlinear flow behaviors in 3D self-affine rough fractures: Lattice Boltzmann simulations. *Adv. Water Resour.* **2016**, *96*, 373–388. [CrossRef]
38. Rong, G.; Tan, J.; Zhan, H.; He, R.; Zhang, Z. Quantitative evaluation of fracture geometry influence on nonlinear flow in a single rock fracture. *J. Hydrol.* **2020**, *589*, 125162. [CrossRef]
39. Grasselli, G.; Wirth, J.; Egger, P. Quantitative three-dimensional description of a rough surface and parameter evolution with shearing. *Int. J. Rock Mech. Min. Sci.* **2002**, *39*, 789–800. [CrossRef]
40. Zimmerman, R.W.; Bodvarsson, G.S. Hydraulic conductivity of rock fractures. *Transp. Porous Media* **1996**, *23*, 1–30. [CrossRef]
41. Wang, Z.; Xu, C.; Dowd, P. A Modified Cubic Law for single-phase saturated laminar flow in rough rock fractures. *Int. J. Rock Mech. Min. Sci.* **2018**, *103*, 107–115. [CrossRef]
42. Zhou, J.Q.; Wang, L.; Li, C.; Tang, H.; Wang, L. Effect of fluid slippage on eddy growth and non-Darcian flow in rock fractures. *J. Hydrol.* **2020**, *581*, 124440. [CrossRef]
43. Forchheimer, P. Wasserbewegung durch Boden. *Zeit. Ver. Deut. Ing.* **1901**, *45*, 1781–1788.
44. Bear, J. *Dynamics of Fluids in Porous Media*; Courier Corporation: Chelmsford, MA, USA, 2013.
45. Zhou, J.Q.; Hu, S.H.; Fang, S.; Chen, Y.F.; Zhou, C.B. Nonlinear flow behavior at low Reynolds numbers through rough-walled fractures subjected to normal compressive loading. *Int. J. Rock Mech. Min. Sci.* **2015**, *80*, 202–218. [CrossRef]
46. Liu, R.; Jiang, Y.; Li, B.; Wang, X. A fractal model for characterizing fluid flow in fractured rock masses based on randomly distributed rock fracture networks. *Comput. Geotech.* **2015**, *65*, 45–55. [CrossRef]

47. Li, B.; Wang, J.; Liu, R.; Wu, F. Deformation and failure of rock fractures under shear compression and nonlinear permeability characteristics. *Eng. Sci. Technol.* **2021**, *53*, 103–112.
48. Zou, L.; Cvetkovic, V. A new approach for predicting direct shear tests on rock fractures. *Int. J. Rock Mech. Min. Sci.* **2023**, *168*, 105408. [CrossRef]
49. Zeng, Z.; Grigg, R. A criterion for non-Darcy flow in porous media. *Transp. Porous Media* **2006**, *63*, 57–69. [CrossRef]
50. Zimmerman, R.W.; Al-Yaarubi, A.; Pain, C.C.; Grattoni, C.A. Non-linear regimes of fluid flow in rock fractures. *Int. J. Rock Mech. Min. Sci.* **2004**, *41*, 163–169. [CrossRef]
51. Liu, R.; Li, B.; Jiang, Y. Critical hydraulic gradient for nonlinear flow through rock fracture networks: The roles of aperture, surface roughness, and number of intersections. *Adv. Water Resour.* **2016**, *88*, 53–65. [CrossRef]

Disclaimer/Publisher's Note: The statements, opinions and data contained in all publications are solely those of the individual author(s) and contributor(s) and not of MDPI and/or the editor(s). MDPI and/or the editor(s) disclaim responsibility for any injury to people or property resulting from any ideas, methods, instructions or products referred to in the content.